

Supplementary Information

Vibrational coherence transfer in the intersystem crossing of a di-platinum complex in solution

Roberto Monni¹, Gloria Capano¹, Gerald Auböck^{1*}, Harry B. Gray², Antonín Vlček^{3,4}, Ivano Tavernelli⁵ and Majed Chergui^{1†}

¹*Ecole Polytechnique Fédérale de Lausanne, Laboratoire de spectroscopie ultrarapide, ISIC and Lausanne Centre for Ultrafast Science (LACUS), FSB, Station 6, CH-1015 Lausanne, Switzerland*

²*Beckman Institute, California Institute of Technology, Pasadena, California 91125, United States*

³*School of Biological and Chemical Sciences, Queen Mary University of London, Mile End Road, London E1 4NS, United Kingdom*

⁴*J. Heyrovský Institute of Physical Chemistry, Czech Academy of Sciences, Dolejškova 3, CZ-182 23 Prague, Czech Republic*

⁵*ITA, IBM, 8803 Rüschlikon, Switzerland*

SI. Materials and Methods

SI.1 Sample preparation

The samples consist of 36 mg of tetra-butyl ammonium (TBA, Bu₄N⁺) salt of tetrakis(μ-pyrophosphito)diplatinate(II), [Pt₂(μ-P₂O₅H₂)₄]⁴⁻ complex (hereafter abbreviated Pt(pop)), dissolved in 20 mL of spectroscopic grade acetonitrile (MeCN from Sigma Aldrich, used as delivered) yielding a concentration of 0.9 mM. At 360 nm, the cross section of the singlet band yields an ~0.3 OD (Optical Density) in a 100 μm flow-cell. A laser fluence of ~1.3 mJ/cm² was used for the measurements.

SI.2 Optical Set-up

The experiments were performed on the 2D UV transient absorption (TA) set-up of the LSU.(1, 2) Briefly, ~0.4 mJ of the output of a 20 kHz, cryogenically-cooled, amplifier (Wyvern, KM

* Now at: CTR Carinthian Tech Research AG; Europastrasse 4/1, 9524 Villach/St. Magdalen, Austria.

† Corresponding author : Majed.chergui@epfl.ch

labs, 780 nm, 50 fs, ~0.6 mJ) are injected into a Non-collinear Optical Parametric Amplifier (NOPA, Topas White from Light Conversion) to provide pulses in the range between 560 nm and 650 nm. The typical output energy is ~15 μJ and ~60% of it is used to generate narrow-band pump pulses. Visible pulses are focused onto a 0.5 mm-thick BBO crystal for frequency doubling, in order to generate the 360 nm pump pulses with typical band-width of ~2 nm and energies of ~150 nJ. The pump pulses are chopped at half the laser repetition rate and focused onto the sample with typical focal spot diameter of 100 μm . In our experiments, 60 fs Full Width at Half Maximum (FWHM) pump pulses were used, leading to an Instrumental Response Function (IRF) of 80 fs FWHM. The visible probe pulses were generated by focusing ~0.5% (~1 μJ) of the remaining output of the amplifier (~0.2 mJ) onto a 5 mm-thick CaF_2 window, in order to generate a white light super-continuum. The probe region in our experiments spans from ~340 nm to ~600 nm. After focusing onto the sample (35 μm diameter at focal spot) the probe is coupled into a 100 μm multi-mode fiber and sent to a spectrometer to be spectrally resolved and detected on a single shot basis by means of a fast CMOS array detector.

SI.3 Data treatment

The data were analyzed by global fit (GF) of several kinetic traces using the fitting function:

$$f(t) = H(t) * \{ G(t) \otimes \left[\sum_i a_i e^{\left(-\frac{t}{\tau_i}\right)} + \sum_j \left(a_j e^{\left(-\frac{t}{\tau_{Dj}} - \frac{(t_0-t)^2}{\text{IRF}^2}\right)} + a_j e^{\left(-\frac{t}{\tau_{Rj}} - \frac{(t_0-t)^2}{\text{IRF}^2}\right)} \right) \sin(\omega_j t + \phi_j) \right] \} \quad (\text{Eq. S1})$$

Where $H(t)$ is the Heaviside step function, $G(t)$ is a Gaussian function (with FWHM equal to the experimental IRF) convoluted with the sum of exponential decays (with amplitude a_i and time-constant τ_i) and exponentially damped sine functions. The t_0 factor is related to the time zero definition, while the IRF value is identified as the FWHM of the $G(t)$ function. In this way, it is possible to account for the population times, through the sum over “ i ”, and for the exponentially damped oscillatory pattern, through the sum over “ j ”. The damped oscillatory pattern is described by the $\sin(\omega t + \phi)$ term multiplied by the damping exponential (first exponential term inside the sum) and another exponential that accounts for the rise (second exponential inside the sum). The damping and rising time-constants are represented by τ_D and τ_R , respectively. The sine functions describe the oscillatory pattern whose frequencies (in cm^{-1}) are retrieved with a very small uncertainty and are cross-checked by Fast Fourier Transforms

(FFT, see below) of the oscillatory patterns as a function of probe wavelength, after subtracting the exponential signals.

Global analysis of the GVD-corrected data-matrix $M(\lambda, t)_{m \times n}$ was performed by Singular Value Decomposition (SVD) technique. The SVD procedure starts from the data matrix $M(\lambda, t)_{m \times n}$ and decomposes the latter in the product of three matrices as:

$$M(\lambda, t) = S(\lambda)_{m \times m} \times W_{m \times n} \times T(t)_{n \times n}^T \quad (\text{Eq. S2})$$

If the data matrix can be described by a linear combination of terms and in the case of pure stochastic noise, the columns present in the $S(\lambda)_{m \times m}$ and $T(t)_{n \times n}^T$ matrices are known as singular spectra (also called “eigenspectra”) and singular kinetic vectors (also called “eigen-traces”) respectively. $W_{m \times n}$ is a matrix that has $w_{ij} = w_{ji} = 0$ while $w_{ii} \neq 0$. The latter entries are also called “singular values” and represent the contribution of each eigenspectrum (and the corresponding eigen-trace) to the data matrix. In the case of noise-free data there are n non-vanishing singular values, while the presence of noise acts as a perturbation of the latter and the respective singular vectors.

The global fit (GF) of the relevant eigen-traces allows retrieving the typical times τ_k with their respective uncertainties and amplitudes a_{ik} . The latter can be used to construct the Decay Associated Spectra (DAS), which give the spectra contribution associated to a given time-constant as:

$$DAS_k(\lambda) = \sum_k a_{ik} w_{ii} U_k(\lambda) \quad (\text{Eq. S3})$$

where $U_k(\lambda)$ is the eigen-spectrum related to the k -th eigen-trace.

III. Results of the Data Analysis:

In the GF of the time traces (containing the exponential and the oscillatory parts) by means of equation S1, all fit parameters were free, except for a long-lived component (fixed at 500 ps) representing the triplet state lifetime of Pt(pop). All fits were convoluted with the experimental IRF. The resulting fit parameters for the exponential and oscillatory parts are given in Table 1 of the main article.

In fitting the kinetic (i.e. exponential) parts, a point of caution needs to be made: the use of 2- or 3-exponentials as done here implies kinetically distinct processes, which may not be the correct physical picture. Furthermore, as can be seen in figure 2B, some of the relaxation

processes may occur over tens of ps, which is not really reflected in our multi-exponential fit. A stretched exponential function may be a better representation of the overall vibrational relaxation kinetics. However, we consider the multi-exponentials fits used here as phenomenologically precise enough to extract the oscillatory components of the time traces. We nevertheless discuss the kinetic times in the context of ISC, vibrational relaxation and dephasing, see § SII.

Coming back to the GF of the data. Figure S2 shows the fits of a set of time traces, obtained using a tri-exponential function with three damped sine functions. Table 1 shows decay times of 700 ± 100 fs and 3.8 ± 0.4 ps. The 700 ± 100 fs time constant reflects the depopulation of the singlet state, which is caused by the ISC to the triplet $^3A_{2u}$ state. Indeed, the latter shows a concomitant rise (τ_R) of the oscillations occurs in the ESA_T , with a time constant of 900 ± 100 fs rise time Figure S2 and Table 1). The ~ 3.5 ps time constant appears most clearly in the rise of the signal at 500 nm (Figure 3 and S3). This rise reflects the growth of the incoherent hot vibrational population, which results from the dephasing of the coherences, convoluted with the vibrational relaxation of the incoherent part.

Finally, Fast Fourier Transforms (FFT) have been performed on the oscillatory parts of the time-wavelength plots after subtracting the exponential parts, as explained in detail in ref. (3). The frequencies retrieved from these FFTs, shown in figure S9, are in excellent agreement with those extracted from the GF.

SIII. Computational methods

The structure of Pt(pop) was optimized in the ground state using the GGA-BLYP(4-6) exchange and correlation functional as implemented in the code Amsterdam Density Functional (ADF 2014).(7-9) Dispersion effects were included adding semi-empirical atom pairwise interactions as described by the DFT-D3 method.(10) Triple-zeta STO basis sets(11) were applied for all the atoms.(11) Scalar relativistic effects were included through the zeroth-order regular approximation (ZORA).(12-14) The optimizations were carried out in acetonitrile (MeCN) solutions. The solvent is described using the implicit solvent model COSMO,(15) as in ref. (16). For each geometry a frequency analysis was performed for assuring that it is a local minimum on the energy surface (no imaginary values).

Although the COSMO model allows taking in account some fundamental solvent effects (stabilization of the frontiers orbitals energy), specific interactions between solute and solvent

can only be included in an explicit solvent model description. To this aim and in order to include temperature effects, we performed QM/MM dynamics. *Ab-initio* molecular dynamics were carried out within the quantum mechanics/molecular mechanics (QM/MM) framework using the Car Parrinello Molecular Dynamics (CPMD) code.(17) The quantum box contains a Pt(pop) molecule (composed of 38 atoms) while the classical box includes 4 Na⁺ ions for compensating the negative charge of the complex and 1624 MeCN molecules. After equilibration, the dynamics were run for 6 ps using Born-Oppenheimer (BO) molecular dynamics. The electronic energy was computed using B3LYP exchange and correlation functional with Dispersion Corrected Atom Centred Potentials (DCACP) correction(18-20) for dispersion forces. The atoms were described employing the Martin-Trouiller pseudopotential and plane waves with cut-off of 90 Ry.(21) In addition, spin-orbit coupling between all excited singlet and triplet states, has been computed at the same steps using the Wang-Ziegler formalism(22) as implemented in the ADF code. The temperature of the quantum system was set to 300 K using a Nose-Hoover thermostat(23, 24) with a coupling frequency of 1200 cm⁻¹ for the quantum part and 2000 cm⁻¹ for the classical region. The simulation was run in the ground state with a time step of 10 a.u. (1.a.u = 0.02419 fs) and the trajectory plotted each 25 steps. A second set of simulations was carried out for Pt(pop) in the excited state. Since the potential energy surfaces of the lowest triplet state and the photo-excited singlet state have the same symmetry and are nearly parallel, the forces acting on the nuclei are the same. In this case we can perform a BO molecular dynamics on the lowest triplet state and extrapolate from the dynamics structural information on the photo-excited singlet state. This reduces considerably the computation cost and makes the excited-state dynamics study for Pt(pop) feasible. The initial configurations for the excited state dynamics were chosen randomly from the ground state dynamics. Each 50 steps the structure of Pt(pop) was extracted from the triplet state trajectory and emission energies from the lowest excited singlet and triplet were computed using the ADF code as was done for the optimized triplet state geometries.

The QM/MM approach(25) is based on the partitioning of the system in a quantum subsystem and in a classical subsystem. The total energy is the sum of the energy of the quantum region, the energy of the classical region and the interaction energy between the two sub-systems:(26)

$$E_{TOT}=E_{QM}+E_{MM}+E_{QM/MM} \quad (\text{Eq. S4})$$

This method, in contrast to implicit solvent models like COSMO, does not describe the solvent as a continuum but as an ensemble of molecules that may interact, through electrostatic and

weak interactions, with the quantum part of the system. Specific solute-solvent interactions, such as hydrogen bonds(27) or exciplex formation,(28) can be described by a QM/MM method but not with an implicit solvent model.

SIV. Discussion of simulation results:

To illustrate the effect of the strong solvation of the T₂ state(s), Figure S6 shows the time evolution of the S₁ and T₂ state energies as well as of the Pt-Pt bond along a trajectory propagated in the T₁(S₁) state, for two different solvents: acetonitrile (a) and ethanol (b). The aim of this figure is by no means to quantitatively account for the experimental ISC rates but to qualitatively show the trends. Indeed, only a single trajectory was simulated for each solvent due to the computational cost of the QM/MM simulations, therefore the present calculations are only indicative as they lack statistical averaging (which would require several tens of simulations to be significant). In Figure S6, the amplitude of the energy fluctuations of the S₁ and T₂ state are large (typically, 0.5 eV), but the main result is the strong shift down in energy of the T₂ state(s) due to solvation, to the point that it (they) come to close resonance with the S₁ state, thus providing a pathway for population flow from the latter. owing a clear correlation to the Pt-Pt bond oscillations, they are much noisier, due to the additional solvent fluctuations. This is clearly seen in the Fourier transforms (FT) of these traces, shown in figure S6. The main peak in the FT of the Pt-Pt trajectory is at ~3.5 THz, which corresponds to the oscillation frequency of this bond. This peak is somewhat present in the FT of the energy trajectories of the S₁ and T₂ states, but these are much noisier, in particular in acetonitrile, due to the solvent fluctuations.

SV. Molecular parameters of the ground and excited states

Table S1: Equilibrium constant and oscillation frequency of the ground and the lowest triplet and singlet states of Pt(pop) obtained from low-temperature steady-state spectroscopic studies and from time-resolved optical studies (references are given in brackets).

State	S₀	T₁	S₁
R _{eq.} (Å)	2.925(29)	2.71(29)	2.7(30)
ν (cm ⁻¹)	116(31)	156(29,	150(34)
	118(32)	31)	149(33)
	119(33)	157(3)	

SVI. Energy of the absorption bands:

Table S2 compiles the energies of the absorption band maxima of Pt(pop) in different solvents along the corresponding ISC times. The solvent shifts with respect to MeCN (which shows the redmost S_1 absorption energy) are shown in parenthesis.

Table S2: Transition energies from the ground state to the lowest singlet and triplet states and to the UV1 and UV2 bands of Pt(pop) in different solvents (see Figure S1), along with the corresponding ISC times reported in ref. (33) and in this work. The numbers in parenthesis represent the shift with respect to the corresponding state energy in MeCN. The last line is the assignment of states based on ref. (16).

Solvent	T₁ cm⁻¹	S₁ cm⁻¹	UV1 cm⁻¹	UV2 cm⁻¹	UV3 cm⁻¹	τ_{ISC} (ps)
Pt(pop)/ Ethyl. Glycol	22075 (169)	27027 (181)	32787 (1341)	36232 (1144)	40900 (414)	30.3
Pt(pop)/EtOH	22173 (267)	27100 (254)	32787 (1341)	36166 (1078)	40984 (498)	25.6
Pt(pop)/H ₂ O	22100 (194)	27174 (328)	32680 (1234)	36298 (1210)	41068 (582)	13.7
Pt(pop)/DMF	21906 (0)	26810 (36)	31949 (503)	34965 (123)		11.0
Pt(pop)/MeCN	21906 (0)	26846 (0)	31446 (0)	35088 (0)	40486 (0)	0.7
Pt(pop)/H ₂ O: glycerol (1:2) (35)						40
[Pt(pop)+2H] ²⁻ (36)		27200 (200)				0.7
Assignement	³ A _{2u}	¹ A _{2u}	a ³ B _u (85%)+ b ¹ B _u (13%)	a ³ B _u (48%)+ b ³ B _u (47%)	d ³ B _u (82%) + c ¹ B _u (10%)	

SVII. Character of the excited states:

Table S3: Energy (eV) and character of the first four singlet and triplet excited states computed at two excited-state configurations, 600 fs and 1800 fs after photoexcitation, by the QM/MM MD in MeCN. Refer to Table S3 and Fig. 5 for the orbitals.

	Configuration at 600 fs		Configuration at 1800 fs	
	Energy	Character	Energy	Character
S ₁	2.4174	95% HOMO → LUMO	2.4034	93% HOMO → LUMO
S ₂	2.6739	96% HOMO → LUMO+1	2.5221	97% HOMO → LUMO+1
S ₃	3.3247	90% HOMO → LUMO+2	3.3255	94% HOMO → LUMO+2
S ₄	3.4275	92% HOMO-1 → LUMO	3.5167	88% HOMO-1 → LUMO
T ₁	2.0698	97% HOMO → LUMO	2.0400	97% HOMO → LUMO
T ₂	2.4064	96% HOMO → LUMO+1	2.2709	96% HOMO → LUMO+1
T ₃	2.9289	97% HOMO → LUMO+2	2.8723	97% HOMO → LUMO+2
T ₄	3.0763	52% HOMO-1 → LUMO 41% HOMO-1 → LUMO+1	3.1544	75% HOMO-1 → LUMO

Table S4: Energy (eV) and nature of the frontier orbitals computed at the triplet state optimized (Opt) geometry as reported in ref. (16) and at two configurations, 600 fs and 1800 fs after photoexcitation, by the QM/MM MD in MeCN. "Opt" stands for the optimized triplet ground state structure.

MO	Opt		600 fs		Energy	1800 fs
	Energy	Contribution	Energy	Contribution		Contribution
HOMO-4	-6.570	10% Pt (p)	-7.202	1% Pt (d), 5% Pt (p)	-7.164	8% Pt (d), 4% Pt (p)
HOMO-3	-6.567	10% Pt (p)	-6.965	1% Pt (d), 8% Pt (p)	-6.964	8% Pt (d), 6% Pt (p)
HOMO-2	-6.552	11% Pt (p)	-6.821	8% Pt (d), 5% Pt (p)	-6.917	9% Pt (d), 8% Pt (p)
HOMO-1	-6.550	11% Pt (p)	-6.487	12% Pt (d), 11% Pt (p)	-6.620	6% Pt (d), 5% Pt (p)
HOMO	-5.588	Pt (dσ*) 64% Pt(d),4% Pt(p)	-5.645	Pt (ds) 59% Pt(d)	-5.681	Pt (dσ*) 64% Pt(d), 3% Pt(p), 12%Pt (s)
LUMO	-1.384	44% Pt (p)	-2.276	23% Pt (d), 11% Pt (p)	-2.317	22% Pt (d), 13% Pt (p)
LUMO+1	-0.176	28% Pt (d)	-1.920	27% Pt (d)	-2.091	30% Pt (d)
LUMO+2	-0.126	30% Pt (d)	-1.473	14% Pt (d), 21% Pt (p)	-1.528	10% Pt (d), 32% Pt(p)
LUMO+3	0.314	5% Pt(d),14% Pt(p), 6% Pt(s)	-0.275	2% Pt (p), 5% Pt(s)	-0.451	11% Pt(p), 4% Pt(s)
LUMO+4	0.866	32%Pt(s)	0.090	8% Pt (p), 2% Pt(s)	-0.053	3% Pt(d),11% Pt(p), 8% Pt(s)

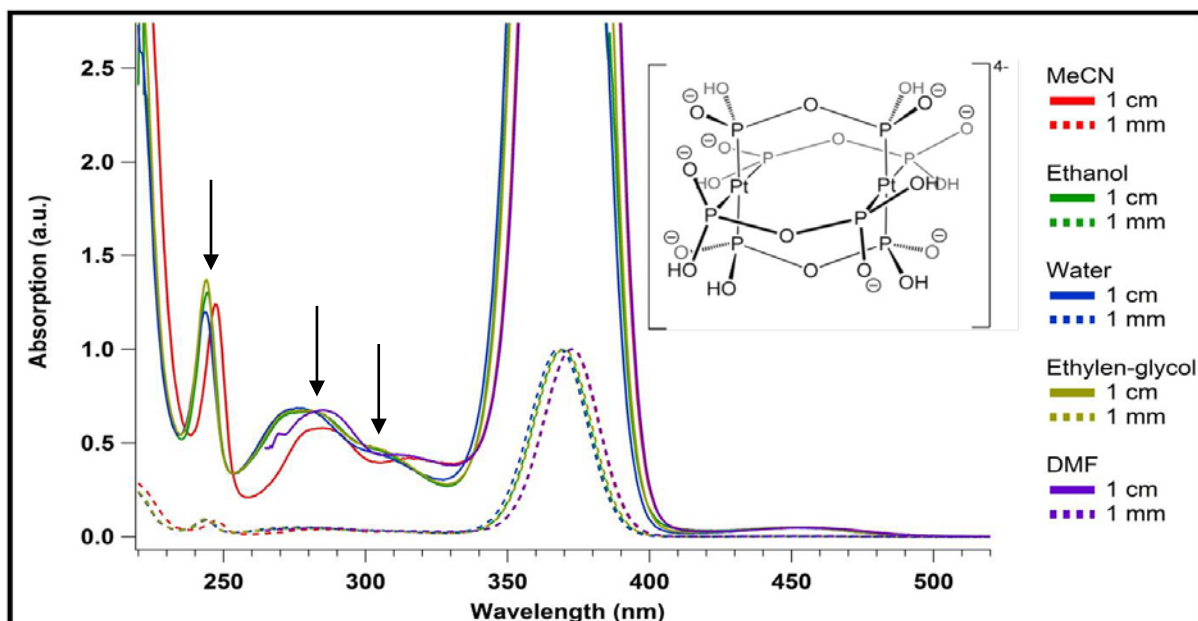


Figure S1: Comparison of the static spectra of Pt(pop) in different solvents. The band positions are summarized in Table S1. The arrows point to the so-called UV bands at: 280-305 nm, 240-250 nm and ~245 nm. Each spectrum was acquired using two different cuvettes (1 mm and 1 cm, respectively). The thick cell was used to enhance the weak features.

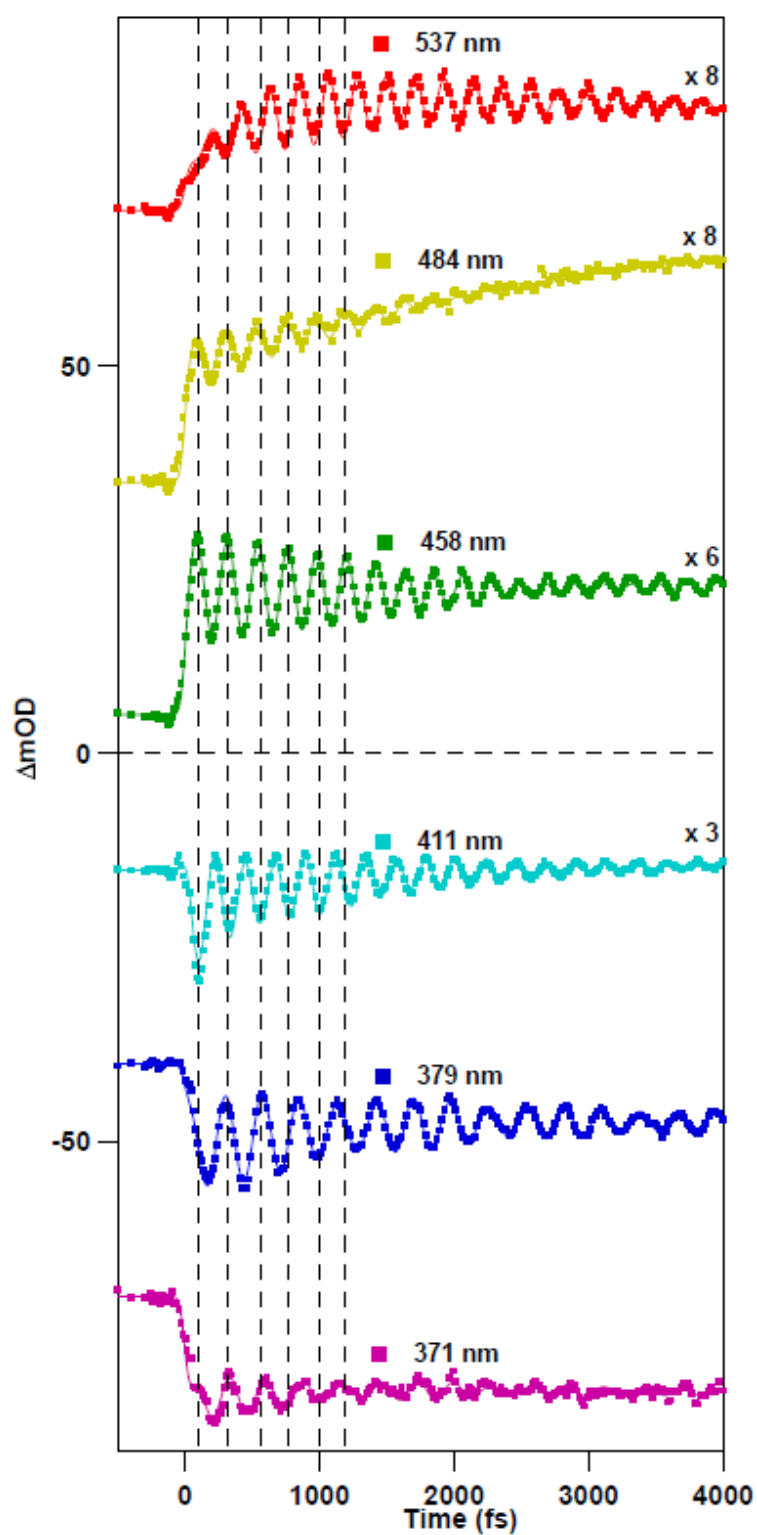


Figure S2: Time traces at different probe wavelengths of Pt(pop) in MeCN excited at 360 nm. The solid lines represent the results of the Global Fit (see text).

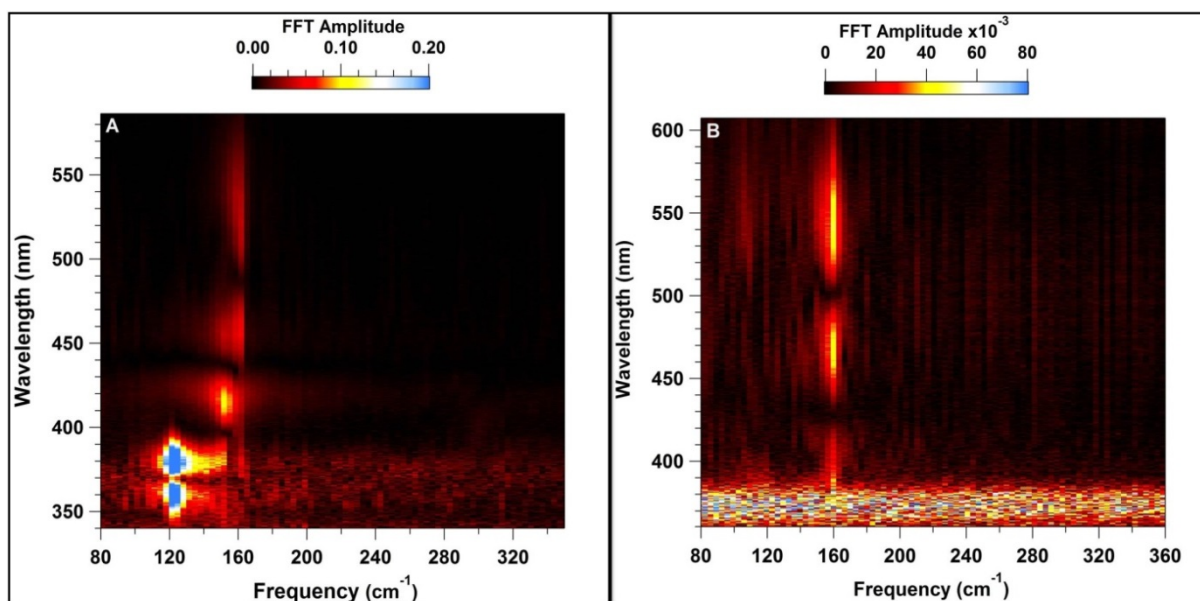


Figure S3: Fast Fourier Transform (FFT) maps of the oscillatory pattern of Ptpop in MeCN upon photoexcitation at 360 nm (A) and 280 nm (B). The 280 nm is reproduced from ref. (3), which also contains the details of the procedure to perform these FFT's.

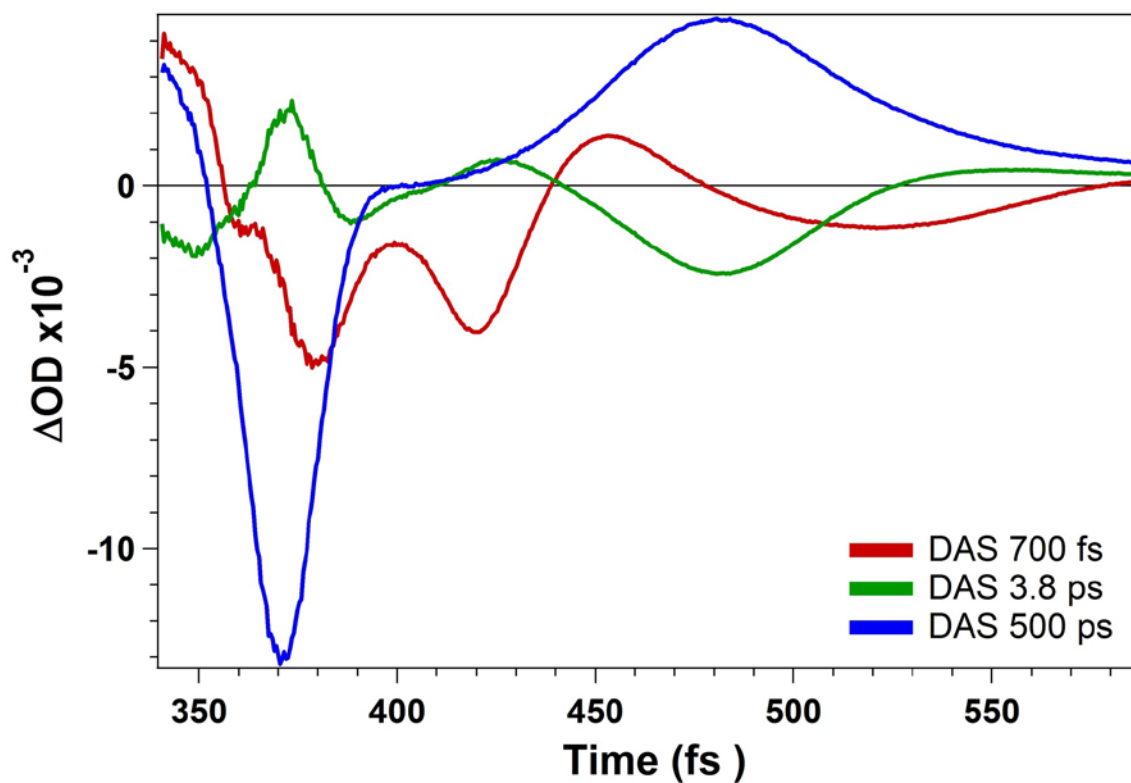


Figure S4: Decay Associated Spectra (DAS) extracted from the time-wavelength plot of Pt(pop) in MeCN upon 360 nm excitation. The minimum at ~ 420 nm in the 700 fs DAS is due to stimulated emission, while the maximum at around 450 nm is due to its ESA. The 375 nm minimum is due to the Ground state bleach overlapped with a strong ESA of the singlet state. Finally, the 500 ps DAS shows only the GSB at 370 nm and the ESA due to the triplet at 470 nm.

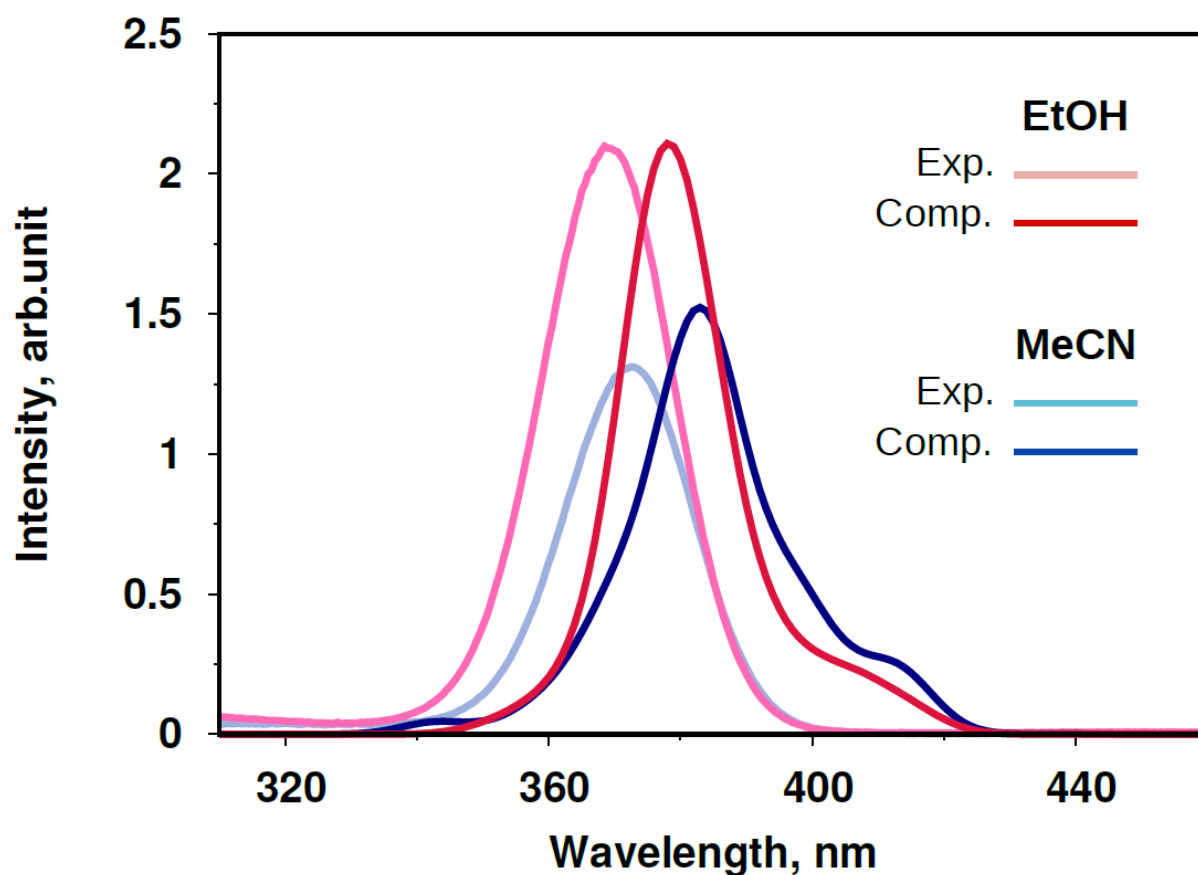


Figure S5: Comparison of the experimental and theoretical absorption spectra of Pt(pop) in MeCN. The computed spectra are evaluated from a ground state simulation over 6 ps and the structures are extracted every 500 a.u. (1 a.u. = 0.02419 fs). Calculations are performed at TDDFT level of theory using the B3LYP functional in the range of the lowest allowed $^1A_{1g} \rightarrow ^1A_{2u}$ transition. The solvent molecules are described with a classical force-field, coupled to the QM system (the Pt(pop) molecule) using the QM/MM coupling scheme. Note that in all subsystems (MM and QM) the nuclei are described classically.

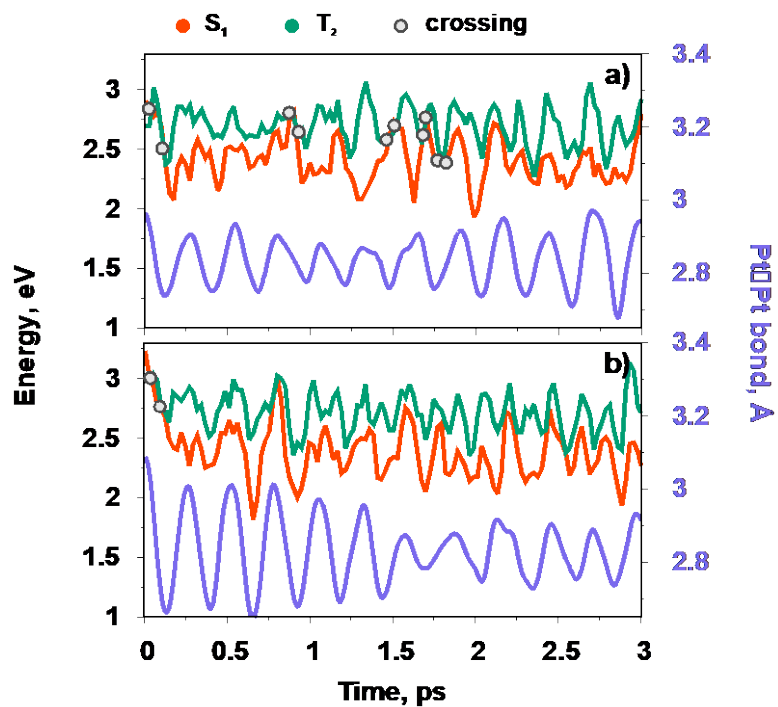


Figure S6: Evolution of the S_1 and T_2 state energies and of the Pt-Pt bond distance as a function of time in two different solvents (upper panel: MeCN, lower panel EtOH). The crossing points between the two electronic states are highlighted by grey circles.

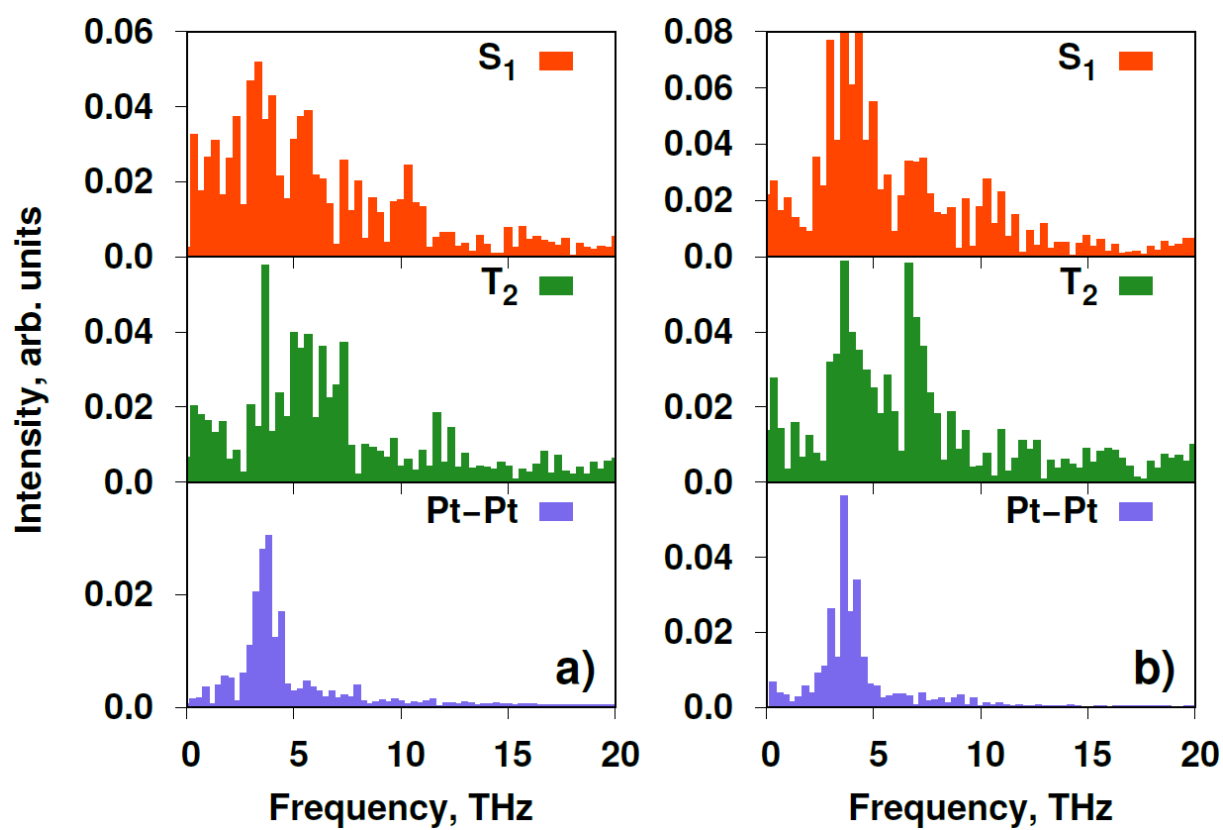


Figure S7: Fourier Transforms of traces shown in figure S6 for: a) acetoneitrile and b) ethanol.

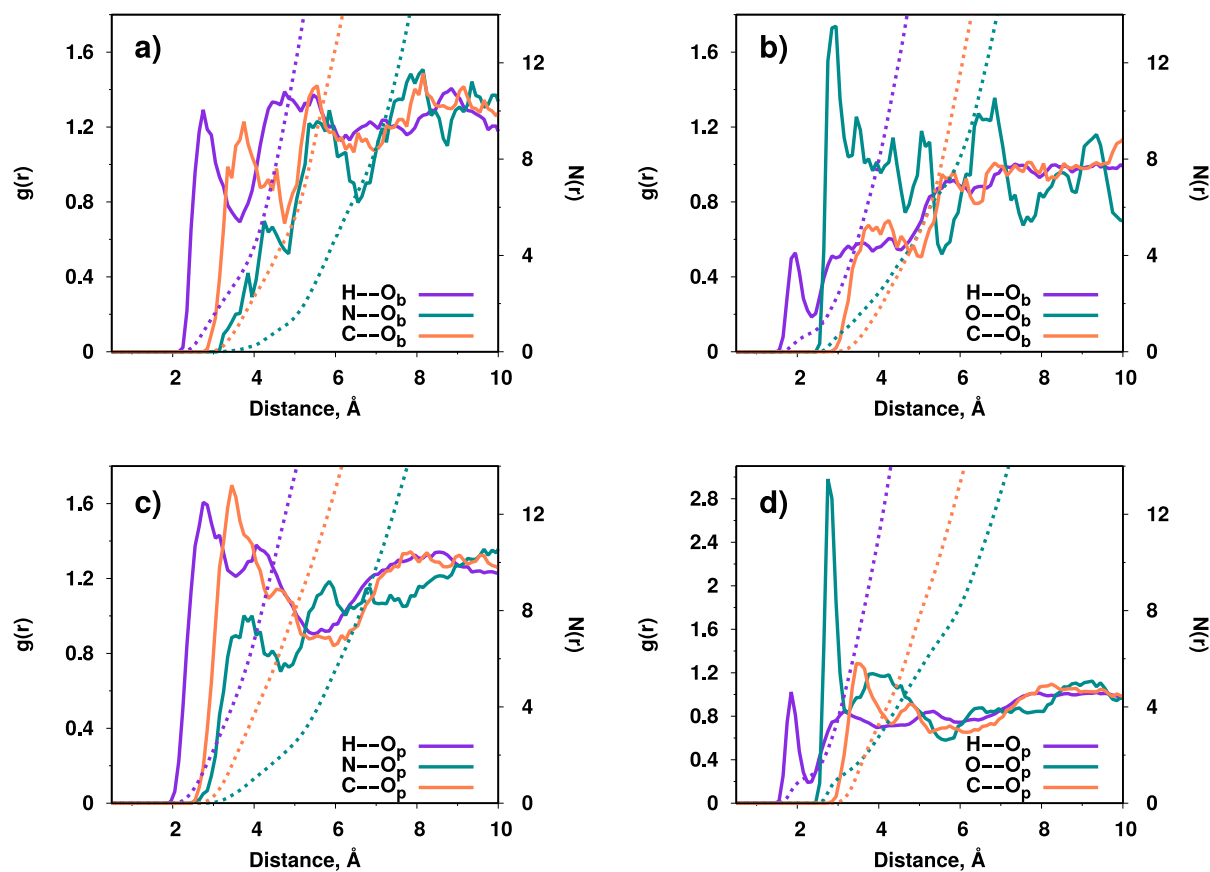


Figure S8: Radial distribution function of the distances between the bridging O (O_b) and polar O (O_p, directly correlated to the Pt atoms) of the Pt(pop) complex and the H, C and N atoms of the acetonitrile solvent molecules (panels a and c, respectively). The corresponding distributions in ethanol are shown in panels b and d. The radial distribution functions are averaged over 6 ps of the QM/MM simulation. Occupation numbers are obtained integrating the radial distribution functions (dashed line, right vertical axis).

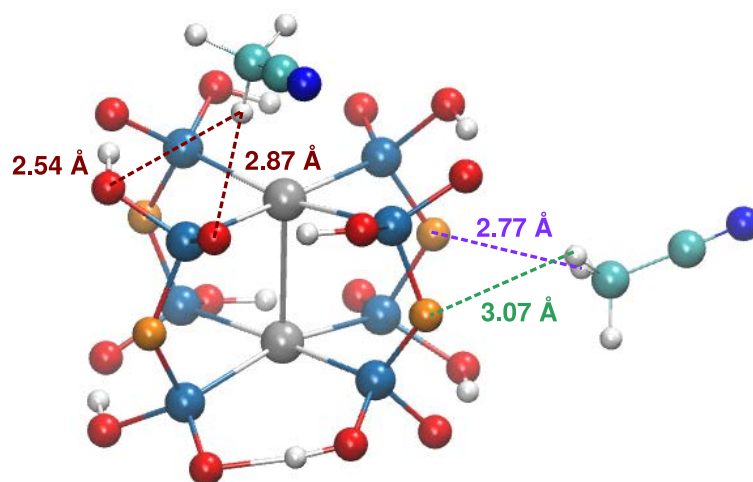


Figure S9: Graphical representation of the Pt(pop) molecule and two acetonitrile molecules in its first solvation interacting with the bridging O atoms (orange) and the polar O atoms (red). This snapshot was taken from the ground state QM/MM simulation of the fully solvated Pt(pop) molecule. All other solvent molecules are removed for clarity.

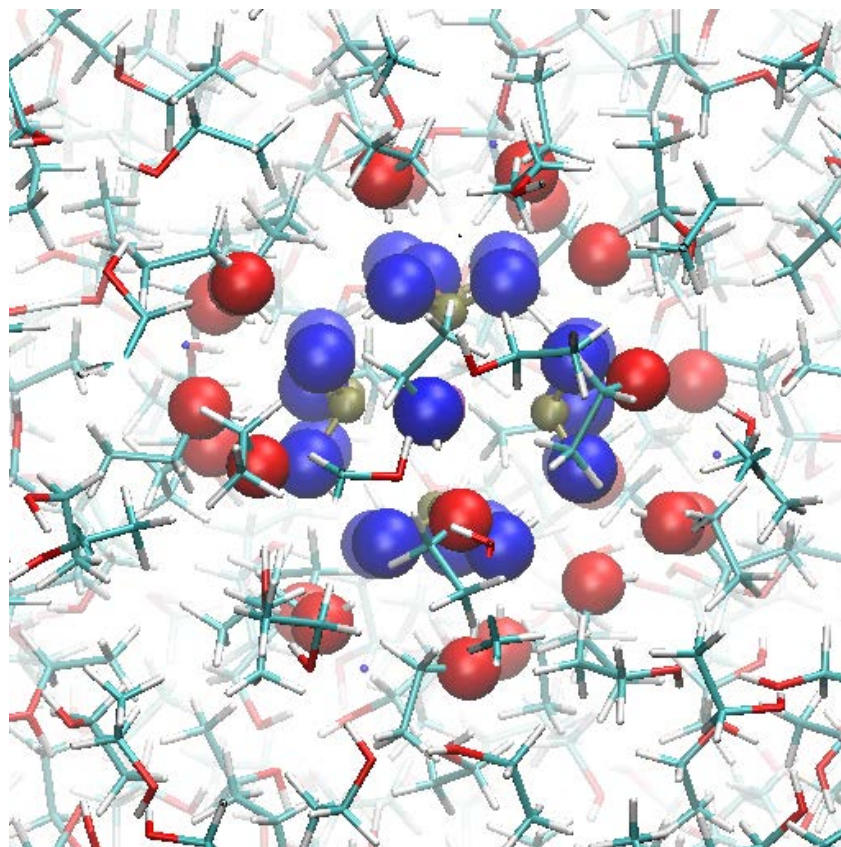


Figure S10: Representation of the first (blue balls) and second (red balls) oxygen solvation shells surrounding the Pt(pop) molecule. This frame (obtained from the QM/MM simulation in the ground state) shows the top view of the Pt(pop) molecule; visible are the 4 Phosphorus atoms in brown while the two, aligned, platinum atoms are masked by the top (central) oxygen atom in blue. The selected atoms (blue and red balls) are responsible for the appearance of the well-structured peaks in the RdF of Figure S8d.

Bibliography

1. Aubock G, *et al.* (2012) Femtosecond pump/supercontinuum-probe setup with 20 kHz repetition rate. *Review of Scientific Instruments* 83(9):093105.
2. Aubock G, Consani C, van Mourik F, & Chergui M (2012) Ultrabroadband femtosecond two-dimensional ultraviolet transient absorption. *Optics Letters* 37(12):2337-2339.
3. Monni R, *et al.* (2017) Conservation of vibrational coherence in ultrafast electronic relaxation: The case of diplatinum complexes in solution. *Chem Phys Lett* 683:112-121.
4. Lee CT, Yang WT, & Parr RG (1988) Development of the Colle-Salvetti Correlation-Energy Formula into a Functional of the Electron-Density. *Physical Review B* 37(2):785-789.
5. Becke AD (1988) Density-Functional Exchange-Energy Approximation with Correct Asymptotic-Behavior. *Phys Rev A* 38(6):3098-3100.
6. Miehlich B, Savin A, Stoll H, & Preuss H (1989) Results Obtained with the Correlation-Energy Density Functionals of Becke and Lee, Yang and Parr. *Chem Phys Lett* 157(3):200-206.
7. te Velde G, *et al.* (2001) Chemistry with ADF. *J Comput Chem* 22(9):931-967.
8. Guerra CF, Snijders JG, te Velde G, & Baerends EJ (1998) Towards an order-N DFT method. *Theor Chem Acc* 99(6):391-403.
9. te Velde Gea (2014) ADF2014, SCM, Theoretical Chemistry (Vrije Universiteit, Amsterdam, The Netherlands).
10. Grimme S, Antony J, Ehrlich S, & Krieg H (2010) A consistent and accurate ab initio parametrization of density functional dispersion correction (DFT-D) for the 94 elements H-Pu. *J Chem Phys* 132(15).
11. Van Lenthe E & Baerends EJ (2003) Optimized slater-type basis sets for the elements 1-118. *J Comput Chem* 24(9):1142-1156.
12. Vanlenthe E, Baerends EJ, & Snijders JG (1993) Relativistic Regular 2-Component Hamiltonians. *J Chem Phys* 99(6):4597-4610.
13. Vanlenthe E, Baerends EJ, & Snijders JG (1994) Relativistic Total-Energy Using Regular Approximations. *J Chem Phys* 101(11):9783-9792.
14. van Lenthe E, Ehlers A, & Baerends EJ (1999) Geometry optimizations in the zero order regular approximation for relativistic effects. *J Chem Phys* 110(18):8943-8953.
15. Pye CC & Ziegler T (1999) An implementation of the conductor-like screening model of solvation within the Amsterdam density functional package. *Theor Chem Acc* 101(6):396-408.
16. Zalis S, Lam YC, Gray HB, & Vlcek A (2015) Spin-Orbit TDDFT Electronic Structure of Diplatinum(II,II) Complexes. *Inorg Chem* 54(7):3491-3500.
17. Andreoni W & Curioni A (2000) New advances in chemistry and materials science with CPMD and parallel computing. *Parallel Comput* 26(7-8):819-842.
18. von Lilienfeld OA, Tavernelli I, Rothlisberger U, & Sebastiani D (2004) Optimization of effective atom centered potentials for London dispersion forces in density functional theory. *Physical Review Letters* 93(15):153004.
19. von Lilienfeld OA, Tavernelli I, Rothlisberger U, & Sebastiani D (2005) Performance of optimized atom-centered potentials for weakly bonded systems using density functional theory. *Physical Review B* 71(19):195119.
20. Lin IC, *et al.* (2007) Library of dispersion-corrected atom-centered potentials for generalized gradient approximation functionals: Elements H, C, N, O, He, Ne, Ar, and Kr. *Physical Review B* 75(20):205131.
21. Troullier N & Martins JL (1991) Efficient Pseudopotentials for Plane-Wave Calculations. *Physical Review B* 43(3):1993-2006.
22. Wang F & Ziegler T (2004) Excitation energies of some d(1) systems calculated using time-dependent density functional theory: an implementation of open-shell TDDFT theory for doublet-doublet excitations. *Molecular Physics* 102(23-24):2585-2595.

23. Nose S (1984) A Unified Formulation of the Constant Temperature Molecular-Dynamics Methods. *J Chem Phys* 81(1):511-519.
24. Hoover WG (1985) Canonical Dynamics - Equilibrium Phase-Space Distributions. *Phys Rev A* 31(3):1695-1697.
25. Lin H & Truhlar DG (2007) QM/MM: what have we learned, where are we, and where do we go from here? *Theor Chem Acc* 117(2):185-199.
26. Laio A, VandeVondele J, & Rothlisberger U (2002) A Hamiltonian electrostatic coupling scheme for hybrid Car-Parrinello molecular dynamics simulations. *J Chem Phys* 116(16):6941-6947.
27. Chandrasekhar J, Shariffskul S, & Jorgensen WL (2002) QM/MM simulations for Diels-Alder reactions in water: Contribution of enhanced hydrogen bonding at the transition state to the solvent effect. *J Phys Chem B* 106(33):8078-8085.
28. Novozhilova IV, Volkov AV, & Coppens P (2003) Theoretical analysis of the triplet excited state of the [Pt-2(H₂P₂O₅)(4)](4-) ion and comparison with time-resolved x-ray and spectroscopic results. *Journal of the American Chemical Society* 125(4):1079-1087.
29. Rice SF & Gray HB (1983) Electronic Absorption and Emission-Spectra of Binuclear Platinum(II) Complexes - Characterization of the Lowest Singlet and Triplet Excited-States of Pt₂(H₂p₂o₅)₄⁴⁻. *Journal of the American Chemical Society* 105(14):4571-4575.
30. Leung KH, Phillips DL, Che CM, & Miskowski VM (1999) Resonance Raman intensity analysis investigation of metal-metal bonded transitions: an examination of the (1)A(2u) <- (1)A(1g) (5d sigma* -> 6p sigma) transition of Pt-2(P₂O₅H₂)(4)(4-). *J Raman Spectrosc* 30(11):987-993.
31. Fordyce WA, Brummer JG, & Crosby GA (1981) Electronic Spectroscopy of a Diplatinum(II) Octaphosphite Complex. *Journal of the American Chemical Society* 103(24):7061-7064.
32. Che CM, Butler LG, Gray HB, Crooks RM, & Woodruff WH (1983) Metal-Metal Interactions in Binuclear Platinum(II) Diphosphite Complexes - Resonance Raman-Spectra of the 1a_{1g}(D-Sigma Star)² and 3a_{2u}(D-Sigma Star P-Sigma Star) Electronic States of Pt₂(P₂o₅h₂)₄⁴⁻. *Journal of the American Chemical Society* 105(16):5492-5494.
33. van der Veen RM, Cannizzo A, van Mourik F, Vlcek A, & Chergui M (2011) Vibrational Relaxation and Intersystem Crossing of Binuclear Metal Complexes in Solution. *Journal of the American Chemical Society* 133(2):305-315.
34. Stiegman AE, Rice SF, Gray HB, & Miskowski VM (1987) Electronic Spectroscopy of D₈-D₈ Diplatinum Complexes - 1a_{2u}(Dsigma Star-]P-Sigma), 3e_u(Dxz,Dyz-]P-Sigma), and 3,1b_{2u}(Dsigma Star-] Dx²-Y²) Excited-States of Pt₂(P₂o₅h₂)₄⁴⁻. *Inorg Chem* 26(7):1112-1116.
35. Milder SJ & Brunschwig BS (1992) Factors Affecting Nonradiative Decay - Temperature-Dependence of the Picosecond Fluorescence Lifetime of Pt₂(Pop)₄(4-). *Journal of Physical Chemistry* 96(5):2189-2196.
36. Kruppa SV, *et al.* (2016) Fragmentation pathways of dianionic [Pt₂(μ-P₂O₅H₂)₄ + X,Y]²⁻ (X,Y = H, K, Ag) species in an ion trap induced by collisions and UV photoexcitation. *Int J Mass Spectrom* 395:7-19.